The Nature of Dense Matter from Multi-Messenger Neutron Star Observations

Satyajit Roy[1] and Andrew W. Steiner[1,2]
[1] *Department of Physics and Astronomy, University of Tennessee, Knoxville, Tennessee 37996, USA and*
[2] *Physics Division, Oak Ridge National Laboratory, Tennessee 37830, USA*

Neutron stars provide a unique laboratory for the study of dense and strongly-interacting matter. Recently, [1] performed the first combined analysis for isolated neutron stars with a well-defined likelihood function and the model reproducing the structure of heavy nuclei. The model went beyond the "minimal cooling" model by varying the EoS. Han et al. (2017) calculated heating curves for soft X-ray transients that agree with the observations. This work continues to combine these and improve upon them with the latest data from Potekhin et al. 2020 for isolated neutron stars while also including LIGO data from GW170817 and recent PREX discoveries. These observations will help constrain the nature of hot and dense matter: in particular nucleonic superfluidity and the composition of dense matter.

INTRODUCTION

Neutron stars are excellent to study strongly-interacting matter as they are much more dense than the atomic nuclei we can probe at laboratories [2]. To fully understand these complex objects, their structure and evolution; we need a model for the dense nuclear matter, explaining the nuclear reactions inside and an equation of state (EoS) that describes the relationship between the pressure and the energy density inside the star. An accurate description of neutron stars requires these models to be grounded in nuclear physics and constrained by multi-messenger observations. The goal is to improve these models of the nuclear physics of neutron star interiors with more observations as they come along.

Ref. [3] analyzed isolated neutron star cooling observations by constructing a "minimal model". This minimal model had as few parameters as possible, presumed a fixed equation of state and assumed that fast cooling processes were ruled out. However these slower cooling processes were later discovered to be insufficient to explain the colder accreting neutron stars observed like SAX J1808 [4]. These colder accreting neutron stars appear to require fast neutrino emission processes like the direct Urca processes: $n \to p + e^- + \bar{\nu}_e$ and $p + e^- \to n + \nu_e$. The direct Urca processes rapidly cool the neutron star because the associated emissivity is enhanced by 5-6 orders of magnitude compared to the minimal cooling models. While fast neutrino cooling processes appear to be required to explain the observational data, nucleonic superfluidity has a dramatic effect on these neutrino emissivities.

Ref. [5] first predicted that neutrons in neutron stars may be superfluid below a certain critical temperature T_c. Superfluidity has three main impacts. First, it exponentially suppresses the specific heat. Second, it exponentially suppresses many cooling processes which would otherwise require the breaking of a Cooper pair. Finally, it creates a new cooling process: the Cooper pair formation neutrino emissivity (see e.g. a recent review of the impact of superfluidity on cooling in Ref. [6].) We discuss this in more detail below.

Previous works Ref. [1] and Ref. [7] provide valuable constraints on the superfluidity and direct Urca process and the interplay between them [8]. This work aims to add new isolated neutron stars data from Ref. [9], LIGO data from GW170817 [10], updated neutron star mass and radius measurements for M30, J0740 and J0030; and the PREX result [11] to get better constraints on the equation of state and the nucleonic superfluidity.

THEORETICAL OVERVIEW

We consider only nucleonic matter and small magnetic fields. We solve the nuclear structure for ^{208}Pb and ^{90}Zr and the stellar structures for our stars. The thermal evolution of these stars are calculated with Dany Page's neutron star cooling code [12]. We employ Bayesian inference (see [1] and [7] and the references therein for detailed descriptions) with either uniform or log-uniform prior distributions for our parameters.

To solve the internal structure of a spherically symmetric neutron star we solve the Tolman-Oppenheimer-Volkov (TOV) equations which are:

$$\begin{aligned} \frac{dP}{dr} &= -\frac{G\epsilon m}{r^2}\left(1+\frac{P}{\epsilon}\right)\left(1+\frac{4\pi P r^3}{m}\right)\left(1-\frac{2Gm}{r}\right)^{-1} \\ \frac{dm}{dr} &= 4\pi r^2 \epsilon \end{aligned} \tag{1}$$

where $\epsilon(r)$, $P(r)$ and $m(r)$ are the energy density, pressure and enclosed gravitational mass at radius r (see [13] and ([14] chapter 10)). These two equations can be solved given an EoS, $P(\epsilon)$, the relation between pressure and energy density for a simple fluid. Different EoSs can have unique and profound impacts on the solutions of these TOV equations.

Probing dense nuclear matter for its EoS is a challenging task and can be categorized into two different approaches: ab initio models and phenomenological models. Ab initio models employ quantum many body interactions with few assumptions and can be typically

systematically improved. On the other hand, ab initio models are often too computationally expensive for larger nuclei. Phenomenological models use more simplifying assumptions and enable faster calculations. Some of these phenomenological models depend on effective interactions and using them we can approximately reproduce nuclear matter properties [15]. A summary of these models can be found in [15]. In our case, we use Relativistic Mean-Field (RMF) models, a phenomenological model of nuclei and nuclear matter. As mentioned in [15], RMF models have been quite successful, describing both nuclei and exotic nuclei (see, the references therein for a review and different RMF parameterizations and their comparisons.

There are the 6 parameters controlling superfluidity, 17 parameters for the relativistic mean-field EoS (see [16] and table 3 in [17]) that we use, parameters describing neutron star masses and envelope properties and parameters for the LIGO data. Assuming these observations are independent of each other, we have a likelihood function that is the product of all the individual likelihoods that are part of our work. In the following sections we will discuss how we do our parameterizations and construct our likelihood.

Nuclei

We make sure our nuclear matter properties are physical and within observed constraints [18]. The quantities we look out for are the saturation density, binding energy of nuclear matter, symmetry energy and compressibility.

The saturation density is the critical density where the central density remains the same even if the system acquires more nucleons. This happens due to the close range repulsive interactions between the nucleons. The saturation density is 0.153 fm^{-3} in Ref. [18] and 0.16 fm^{-3} in Refs. [19, 20]. We restrict the saturation density $0.14\ \text{fm}^{-3} < n_0 < 0.17\ \text{fm}^{-3}$.

At saturation density, the system is at its ground state energy and the energy per baryon required to form the system is its binding energy , E/A. The value is -16.3 MeV/nucleon in Ref. [18] and -16.0 MeV/nucleon in Refs. [19, 20]. We reject all models for which the binding energy is outside the range between -17 to -15 MeV.

Stable lower mass nuclei often prefer nearly equal neutron and proton numbers (symmetric nuclear matter) while heavy nuclei neutron numbers start taking over the protons due to Coulomb repulsion resulting in neutron rich nuclei. This asymmetry results in variation of the binding energy and is represented by the symmetry energy. The symmetry energy coefficient (arising from the isospin asymmetry) S is $31 - 33$ MeV according to Ref. [21], 32.5 MeV according to Ref. [18] and Refs. [19, 20]. At the nuclear saturation density we restrict the symmetry energy $S < 36$ MeV and the slope of the symmetry energy$L < 80$ MeV [22]. The symmetry energy S can be defined by [13]:

$$S(n_B, \delta) \equiv \frac{1}{2n_B} \frac{\partial^2 \epsilon}{\partial \delta^2} \tag{2}$$

where n_B is the total baryon number density, $\delta \equiv (n_n - n_p)/n_B$ is the asymmetry and $\epsilon \equiv (n_B - n_0)/3n_0$ with n_0 as the nuclear saturation density. The slope of the symmetry energy L is defined as [13]:

$$L(n_B, \delta) \equiv 3n_B \frac{\partial S(n_B, \delta)}{\partial n_B} \tag{3}$$

The nuclear incompressibility K at saturation density dictates how the energy density varies with changes in pressure. it is around 234 MeV according to Ref. [18], while Ref. [19] predicts K at 265 MeV [20]. We constrain K between 220-260 MeV [23]. K is defined as [13]:

$$K(n_B, \delta) \equiv 9 \left(\frac{\partial P}{\partial n_B} \right) = 9n_B \left(\frac{\partial^2 \epsilon}{\partial n_B^2} \right) \tag{4}$$

Charge radius is a fundamental nuclear property that connects effective interactions with the structure of a nuclei and is dependent on the rms radius of proton. The rms radius is defined to be [24]:

$$R_{\text{rms}}^2 = 4\pi \int r^4 \rho(r) dr \tag{5}$$

where $\rho(r)$ is the density of protons. When this density is replaced by the charge density, we get the charge radius. The charge density according to [24]:

$$\rho_{\text{ch}}(r) = \int dr' \rho_{\text{cd}}(r - r') \rho_P(r') \tag{6}$$

where $\rho_{\text{cd}}(r)$ is the charge distribution of protons and $\rho_P(r)$ is point proton density.

The likelihood function for nuclear structure data is the product of two-dimensional Gaussian for the binding energy and charge radius of ^{208}Pb and ^{90}Zr (see[1]).

Skin thickness of the nuclei is the difference between the rms radius of neutrons and protons [25]:

$$R_{\text{skin}} = R_{\text{rms},n} - R_{\text{rms},p} \tag{7}$$

The recent measurement of the parity-violating asymmetry A_{PV} in ^{208}Pb by the PREX-2 collaboration (see [26] provides a constraint to the skin-thickness (estimated 0.283 ± 0.071 fm). For our case, this adds another Gaussian for the skin-thickness to our likelihood and the total

likelihood contribution from the nuclei looks like:

$$\mathcal{L}_{\rm nuclei} = \exp\left\{\left[-\frac{\left(E_{\rm Zr}-\tilde{E}_{\rm Zr}\right)^2}{\left(0.02\tilde{E}_{\rm Zr}\right)^2}-\frac{\left(R_{\rm Zr}-\tilde{R}_{\rm Zr}\right)^2}{\left(0.02\tilde{R}_{\rm Zr}\right)^2}\right]\right\} \times \exp\left\{\left[-\frac{\left(E_{\rm Pb}-\tilde{E}_{\rm Pb}\right)^2}{\left(0.02\tilde{E}_{\rm Pb}\right)^2}-\frac{\left(R_{\rm Pb}-\tilde{R}_{\rm Pb}\right)^2}{\left(0.02\tilde{R}_{\rm Pb}\right)^2}\right]\right\} \times \exp\left\{-\frac{\left(R_{\rm skin}-\tilde{R}_{\rm skin}\right)^2}{\left(0.02\tilde{R}_{\rm skin}\right)^2}\right\} \quad (8)$$

where E_i and $\tilde{E}_i$ are the calculated and the observed binding energies and R_i and $\tilde{R}_i$ are the calculated and observed charge radius respectively for ^{208}Pb and ^{90}Zr. $R_{\rm skin}$ and $\tilde{R}_{\rm skin}$ are the calculated and experimental skin-depth of ^{208}Pb.

Neutron Stars

Neutron stars are small and compact stars of mass ∼1.0-2.0 $M_\odot$ and radius ∼ 10-12 km. Fig. 1 shows neutron star structure at a glance. A neutron star can be broadly structured into having three regions, an atmosphere, a crust and a core. Briefly we can say the atmosphere is the thinnest region at the surface and it is mostly made out of hydrogen, helium or carbon depending on the age of the star. The crust is the region that resides between the atmosphere and the core and it can be sub-divided into two sections, an outer region made of ions and electrons and an inner region made of electrons, free neutrons and neutron rich nuclei [27, 28]. Beneath the crust lies the neutron star core that can also be categorized into two sections, the outer core, made out of mostly neutrons, protons and electrons and an inner core with higher density that can have exotic matter with the standard nuclear matter. The exact physics of inner core still have not been fully explained to this date. For a detailed summary see Refs: [29, 30].

We have three types of neutron stars to work with. Isolated neutron stars (INS) that cool via neutrino and photon emissions, soft X-ray transients (SXRT) that are thermally accreting neutron stars and quiescent low mass X-ray binaries (QLMXB) with the partially known mass-radius data from observations.

The masses of these stars are parameterized by m_f, the mass fraction, defined by, $m_f \equiv (M-1)/(M_{\rm max}-1)$, where M is the stellar mass and $M_{\rm max}$ is the maximum mass of a star allowed from solving the TOV-equations using our particular EoS. Naturally m_f takes values between 0 and 1 as we consider 1 $M_\odot$ to be the lowest mass possible for a neutron star.

The border between the envelope and outer crust is called the boundary and the effective temperature of the star T_e is related to this boundary temperature T_b like [31]:

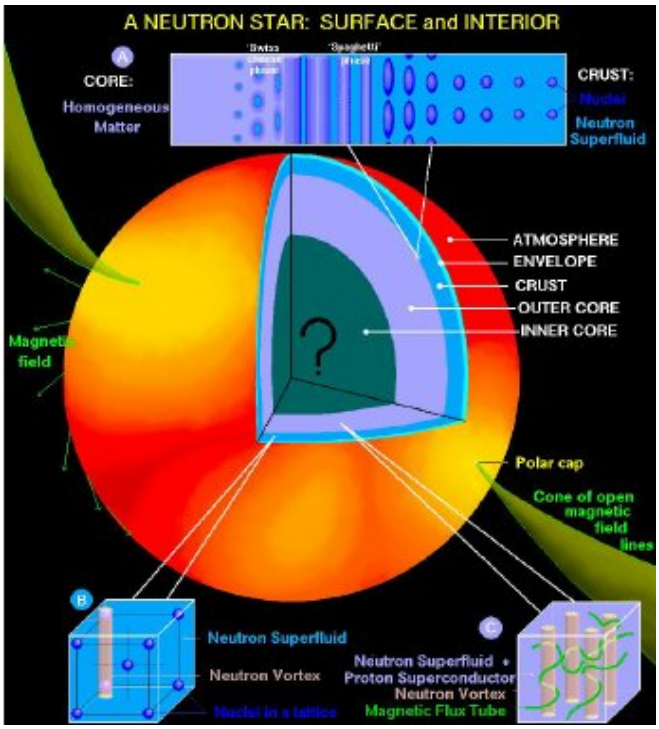

FIG. 1. Neutron star structure.

$$T_e = 0.87\times10^6 (g_{s14})^{1/4}(T_b/10^8{\rm K})^{0.55} \quad (9)$$

where g_{s14} is surface gravity g_s measured in 10^{14} cgs units. As the $T_e - T_b$ relationship is not dependent on the stars M or R explicitly, different envelope models have less drastic effects on the cooling of a neutron star [3]. In our case, just like the minimal cooling model, T_e is related to the internal temperature T through a power-law model $T_e \propto T^{0.5+\alpha}$ with $\alpha \ll 1$ which is really a simplification of the equation above.

For our stars depending on their age, they can either have a light element envelope (H, He) or a heavy element envelope (C). INSs usually have their atmosphere from natural sedimentation process after the supernova explosion while SXRTs and QLMXBs usually might accrete hot matter that accumulates onto their surface creating a light element layer on top of them. Stars with a lighter envelopes cool faster than stars with heavier envelopes due to better heat transport [3]. We parameterize the envelope as η and it takes values from 10^{-7} to 10^{-17}, larger η represents the presence of more light elements in the envelope [32]. We choose fixed $\eta = 10^{-17}$ for stars older than 10^5 years or stars with spectra well fit by a black body spectrum as described in [9]. The cooling code computes eighteen different cooling curves, for six masses ($m = 1.0, 1.2, 1.4, 1.6, 1.8, 2.0\,{\rm M}_\odot$) and three η values ($\eta = 10^{-7}, 10^{-12}, 10^{-17}$). Results for other com-

binations of m and η are obtained through linear interpolation.

Neutron star cooling

Neutron stars are born from supernova explosions of large stars and they cool down via neutrino and photon emissions [30]. The cooling is affected by various factors like the rate of neutrino emissions, the heat capacity of the stellar interior etc. which in turn depend greatly on the EoS and superfluidity inside the star. The envelope also plays a crucial role in reheating due to accretion. Considering a spherically symmetric star and temperature independent interior [33], for a given EoS, one can solve the general relativistic equations of thermal evolution obtained by Thorne (1977) [30] which are the energy balance and heat transport equations [3]:

$$\frac{e^{-\lambda-2\Phi}}{4\pi r^2}\frac{\partial}{\partial r}(e^{2\Phi}L_r) = -Q_\nu + Q_h - \frac{C_v}{e^\Phi}\frac{\partial T}{\partial t} \tag{10}$$

and

$$\frac{L_r}{4\pi\kappa r^2} = e^{-\lambda-\phi}\frac{\partial}{\partial r}(Te^\Phi) \tag{11}$$

where L_r is the luminosity at radius r. The emissivities Q_ν and Q_h are from neutrino and reheating respectively. Heat capacity is C_v and κ is the thermal conductivity. The functions $\phi(r)$ and $\lambda(r)$ are the metric functions described in [30].

After an initial thermal relaxation era after being born, The neutron star is isothermal throughout and the cooling is dominated early via neutrino emission processes and later via photon emission. We calculate the cooling to get the cooling curves $T_s^\infty(t)$ [or $L_\gamma^\infty(t)$] and compare them with observations. Simplifying the problem, $C_v = CT$ and we can write the neutrino and photon luminosities as [12]:

$$L_\nu = NT^8 \text{ and } L_\gamma \equiv 4\pi R^2\sigma_{SB}T_e^4 = ST^{2+4\alpha} \tag{12}$$

and the energy balance equation boils down to:

$$C_v\frac{dT}{dt} = -L_\gamma - L_\nu \tag{13}$$

Neutrino cooling era ($L_\nu \gg L_\gamma$): The neutron star is cooled via various neutrino emission processes, the strongest of them arising from its core.

$$\frac{dT}{dt} = -\frac{N}{C}T^7 \to t - t_0 \propto \left[\frac{1}{T^6} - \frac{1}{T_0^6}\right] \tag{14}$$

where T_0 is the initial temperature at time t_0. For $T \ll T_0$, this gives

$$T \propto t^{-\frac{1}{6}} \text{ and } T_e \propto t^{-\frac{1}{12}} \tag{15}$$

Photon cooling era ($L\nu \ll L_\gamma$): After the neutrino emission era, the star is cooled by photon emission from its surface which in turn affects the internal temperature of the star [30].

$$\frac{dT}{dt} = -\frac{N}{S}T^{1+\alpha} \to t - t_0 \propto \left[\frac{1}{T^\alpha} - \frac{1}{T_0^\alpha}\right] \tag{16}$$

and this gives:

$$T \propto t^{-1/\alpha} \text{ and } T_e \propto t^{-1/2\alpha} \tag{17}$$

as can be seen, in this later stage the composition of the atmosphere really matters and it affects how the star cools.

Neutrino emission processes

The various types of neutrino emission processes that can occur in a neutron star can be summarized in fig. 2. These processes can be broadly categorized into two sec-

Name	Process	Emissivity (erg cm^{-3} s^{-1})	
Modified Urca cycle (neutron branch)	$n+n \to n+p+e^-+\bar{\nu}_e$ $n+p+e^- \to n+n+\nu_e$	$\sim 2\times10^{21}\, R\, T_9^8$	Slow
Modified Urca cycle (proton branch)	$p+n \to p+p+e^-+\bar{\nu}_e$ $p+p+e^- \to p+n+\nu_e$	$\sim 10^{21}\, R\, T_9^8$	Slow
Bremsstrahlung	$n+n \to n+n+\nu+\bar{\nu}$ $n+p \to n+p+\nu+\bar{\nu}$ $p+p \to p+p+\nu+\bar{\nu}$	$\sim 10^{19}\, R\, T_9^8$	Slow
Cooper pair formations	$n+n \to [nn]+\nu+\bar{\nu}$ $p+p \to [pp]+\nu+\bar{\nu}$	$\sim 5\times10^{21}\, R\, T_9^7$ $\sim 5\times10^{19}\, R\, T_9^7$	Medium
Direct Urca cycle (nucleons)	$n \to p+e^-+\bar{\nu}_e$ $p+e^- \to n+\nu_e$	$\sim 10^{27}\, R\, T_9^6$	Fast
Direct Urca cycle (Λ hyperons)	$\Lambda \to p+e^-+\bar{\nu}_e$ $p+e^- \to \Lambda+\nu_e$	$\sim 10^{27}\, R\, T_9^6$	Fast
Direct Urca cycle (Σ^- hyperons)	$\Sigma^- \to n+e^-+\bar{\nu}_e$ $n+e^- \to \Sigma^-+\nu_e$	$\sim 10^{27}\, R\, T_9^6$	Fast
π^- condensate	$n+ < \pi^- > \to n+e^-+\bar{\nu}_e$	$\sim 10^{26}\, R\, T_9^6$	Fast
K^- condensate	$n+ < K^- > \to n+e^-+\bar{\nu}_e$	$\sim 10^{25}\, R\, T_9^6$	Fast
Direct Urca cycle (u-d quarks)	$d \to u+e^-+\bar{\nu}_e$ $u+e^- \to d+\nu_e$	$\sim 10^{27}\, R\, T_9^6$	Fast
Direct Urca cycle (u-s quarks)	$s \to u+e^-+\bar{\nu}_e$ $u+e^- \to s+\nu_e$	$\sim 10^{27}\, R\, T_9^6$	Fast

FIG. 2. The different neutrino emission processes and their emissivities form Dany Page's presentation at the 2022 JINA-INT workshop.

tions, slow ones and fast ones. Their emissivities can be written as [30]

$$Q_{\text{slow}} \propto T_9^8,\ Q_{\text{fast}} \propto T_9^6, \tag{18}$$

where $T_9 = T/(10^9\text{ K})$. The direct Urca process is one of fast neutrino emission processes that is basically β and inverse β decays when only nuclear matter is concerned [12].

$$n \to p + e^- + \bar{\nu}_e \text{ and } p + e^- \to n + \nu_e \tag{19}$$

Just like every other reactions, energy and momentum need to be conserved by these equations. The momentum conservation gives us the the famous triangle rule:

$$p_{F,n} < p_{F,p} + p_{F,e} \tag{20}$$

Now the number density is related to the Fermi-momentum by $n_i = \frac{k_{F,i}^3}{3\pi^2}$. This implies:

$$n_n^{1/3} \leq n_p^{1/3} + n_e^{1/3} = 2n_p^{1/3} \tag{21}$$

which provides the minimum proton fraction required for direct Urca to happen:

$$x_{p,\min} \equiv \frac{n_p}{n_n + n_e} \geq \frac{1}{9} \approx 11\% \tag{22}$$

Apart from direct Urca process there are two more neutrino emission processes that are particularly interesting to us, the modified Urca process and the pair-breaking formation (PBF). When the proton fraction is not large enough to allow for direct Urca, the momentum conservation is not met. However by adding a spectator neutrino, a different reaction takes place that emits neutrino and anti-neutrinos as a result. this is the modified Urca process [12].

$$\begin{aligned} n + n' &\to p + n' + e^- + \bar{\nu}_e \\ p + n' + e^- &\to n + n' + \nu_e \end{aligned} \tag{23}$$

However this has much lower emissivity compared to direct Urca ($\sim 10^{-6}\epsilon_{\rm DU}$). Muons can appear in these reactions when their chemical potential is of the order of their mass and this produces similar reactions with electrons being replaced by the Muons. For detailed descriptions and emissivity rates take a look at [3]. Exotic matter like hyperons can also be in this equations if the necessary criteria is met [12].

There is one other neutrino emission process that is important is the pair breaking formation (PBF). We will discuss this in the superfluidity section.

The Neutron star cooling code

NSCool [12] solves the thermal evolution equations of a spherically symmetric star considering a fully general relativistic case with the necessary cooling and heating mechanisms giving the user the temperature or luminosity profiles of the star along with all the necessary physics outputs. It requires the initial boundary conditions and the physics inputs and an initial temperature profile of the star. The star is discretized in the radial dimension from 0 to a value $i_{\max}$. While luminosities are defined at the even indices, temperatures are defined at the odd indices in an alternating manner. The energy balance and heat transport equations from earlier can be summarized as:

$$\begin{aligned} \frac{d\mathcal{T}}{dt} &= F\left(Q_h, Q_\nu, C_v; \frac{d\mathcal{L}}{dr}\right) \\ \mathcal{L} &= G\left(\kappa, \frac{d\mathcal{T}}{dr}\right) \end{aligned} \tag{24}$$

where

$$\mathcal{T} \equiv e^{\phi} T \text{ and } \mathcal{L} \equiv e^{2\phi} L \tag{25}$$

These partial differential equations are then provided with the boundary conditions: 1. At the center of the star there is no point source or sink of energy: $\mathcal{L}(r=0,t) \equiv 0$. 2. At the surface of the star: $\mathcal{L} = 4\pi R_\infty^2 \sigma_{SB} T_{e,\infty}^4$, where T_e is the surface temperature.

Then the star is evolved step by step in time through iterations and new $\mathcal{T}$ and $\mathcal{L}$ at time $t + dt$ are computed from old $\mathcal{T}^{\rm old}$ and $\mathcal{L}^{\rm old}$ at time t assuming we know them beforehand (this is why an initial temperature profile is needed).

$$\begin{aligned} \frac{d\mathcal{T}}{dt} = F\left(\mathcal{T}, \frac{d\mathcal{L}}{dr}\right) &\to \mathcal{T} = \mathcal{T}^{\rm old} + dt.F\left(\mathcal{T}, \frac{d\mathcal{L}}{dr}\right) \\ \mathcal{L} = G\left(\mathcal{T}, \frac{d\mathcal{T}}{dr}\right) &\to \mathcal{L} = G\left(\mathcal{T}, \frac{d\mathcal{T}}{dr}\right) \end{aligned} \tag{26}$$

Doing this for every time step then gives us the thermal and luminosity evolution profile of the star that we are looking for

$$(\mathcal{T}_i^{(0)}, \mathcal{L}_i^{(0)}) \to (\mathcal{T}_i^{(1)}, \mathcal{L}_i^{(1)}) \to (\mathcal{T}_i^{(2)}, \mathcal{L}_i^{(2)}) \to ... \tag{27}$$

where i is the appropriate even and odd indices for luminosities and temperatures. A guess value of $(\mathcal{T}_i, \mathcal{L}_i)$ are taken in to see if it solves the equations for $(\mathcal{T}_{i+1}, \mathcal{L}_{i+1})$ and they are corrected consecutively until the equations are solved. This gives us the k^{th} to $(k+1)^{th}$ iteration, with corrections $\delta\mathcal{T}_i^{(k)}$ and $\delta\mathcal{L}_i^{(k)}$:

$$\begin{aligned} \mathcal{T}_i^{(k)} \to \mathcal{T}_i^{(k+1)} &= \mathcal{T}_i^{(k)} + \delta\mathcal{T}_i^{(k)} [i = 1, 3, 5, ...] \\ \mathcal{L}_i^{(k)} \to \mathcal{L}_i^{(k+1)} &= \mathcal{L}_i^{(k)} + \delta\mathcal{L}_i^{(k)} [i = 0, 2, 4, ...] \end{aligned} \tag{28}$$

This entire brute force method is accelerated by using Henyey scheme. Solving these equations at all of these indices are treated as a multi-dimensional problem that is solved using Newton-Rhapson method. The energy balance and the heat transport equations can be rewritten as:

$$\begin{aligned} \phi(\mathcal{T}) &= \mathcal{T} - \mathcal{T}^{\rm old} - dt.F\left(\mathcal{T}, \frac{d\mathcal{L}}{dr}\right) = 0 \\ \phi(\mathcal{L}) &= \mathcal{L} - G\left(\mathcal{T}, \frac{d\mathcal{T}}{dr}\right) = 0 \end{aligned} \tag{29}$$

and the iteration goes like:

$$X^{k+1} = X^k - [D\phi(X^k)]^{-1} \times \phi(X^k) \tag{30}$$

for luminosity and temperature alternatively (X stands for luminosity or temperature depending on the index k and D is the derivative matrix of ϕ).

These iterations are continued until the corrections are small enough:

$$\begin{aligned} \mathrm{Max}_{i=1,3,5,\ldots}\left(\frac{\delta\mathcal{T}_i^{(k)}}{\mathcal{T}_i^{(k)}}\right) &< \epsilon_T \text{ and} \\ \mathrm{Max}_{i=0,2,4,\ldots}\left(\frac{\delta\mathcal{L}_i^{(k)}}{\mathcal{L}_i^{(k)}}\right) &< \epsilon_L \end{aligned} \tag{31}$$

The code is really fast and an accuracy of the order of 10^{-10} can be achieved within 5 iterations.

Superfluidity

Neutron stars become superfluid below $T_c(\rho)$ and this is because there is a gap $2\Delta(T)$ near the Fermi energy for the single particle excitations for the nucleons. From BCS theory, below T_c the nucleons form Cooper pairs to populate the higher energy state and emit a neutrino antineutrino pair in the process.

$$\begin{aligned} p + p &\to [pp] + \nu + \bar{\nu} \\ n + n &\to [nn] + \nu + \bar{\nu} \end{aligned} \tag{32}$$

This pairing can occur in $^1S_0$ channel for both neutrons and protons at lower energies and can happen in $^3P_2$ channel for neutrons at higher energies. The gap function at zero temperature is related to the critical temperature by [6]:

$$\Delta(T=0) \sim 1.75 k_B T_c \tag{33}$$

These pairing can have tremendous effects on neutron star cooling. The specific heat and the neutrino emissivity from the predominant neutrino emission processes are suppressed exponentially as a function of the gap while the governing neutrino emissions come from the pair-breaking process which is also a lot weaker compared to the direct Urca emissivity ($\sim 10^{-6}\epsilon_{\rm DU}$). This PBF emissivity is at its strongest just below T_c and it gets weaker as the star cools down.

As the calculations of the superfluid gap has uncertainties in them as differenct models like BCS, C86, C93 or A provide different results as can be seen in fig. 3 (see Ref. [30] for more details), we assume that these gaps can be approximated by a Gaussian of the Fermi momentum:

$$T_c(k_F) = T_{c,\rm peak} \exp\left[\frac{(k_F - k_{F,\rm peak})^2}{2\Delta k_F^2}\right] \tag{34}$$

while we parameterize the height (critical temperature) $T_{c,\rm peak}$, the mean (peak-Fermi momentum) $k_{F,\rm peak}$ and the width Δk_F of the Gaussians for both neutrons and protons separately (giving us total six parameters for our

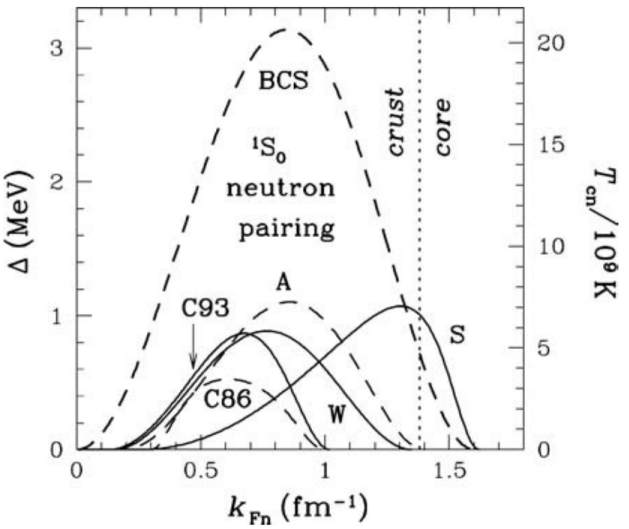

FIG. 3. Different gap models from figure 9 in Ref. [30].

superfluidity) and allow MCMC to choose the values that describe the model well. We apply the appropriate constraints explained in [32] and allow the enhanced cooling processes discussed in [3, 34].

Isolated neutron stars

For isolated neutron stars, we follow [9] and use the data set provided therein and eventually updated in [35]. PSR J1836+5925 (GRO J1837+59), PSR J1819-1458, RX J0420.0-5022, RX J0806.4-4123, RX J2143.0+0654, PSR B0531+21, PSR J2043+2740, PSR B2224+65, PSR B0114+58 (J0117+5914), PSR B0943+10 (J0946+0951), PSR B1133+16 (J1136+1551), PSR J1154-6250, PSR B1929+10 (J1932+1059) were ignored as they provide only upper limits for either temperature or luminosity or both in figure 2 in [9]. Stars PSR J0007+7303 and PSR B1727-47 (J1731-4744) were included as representatives of the luminosity upper limit stars. Fig. 4 shows the luminosity L_γ^∞ plotted against ages t from [9] compared with theoretical cooling curves for INSs with different masses (coded with color), non-accreted (solid curves) and accreted (dashed curves) blanketing envelopes.

X-ray based observatories like Chandra can detect the pulses coming from these stars and sometimes the proper motion data of these stars as well. The pulse period P and its derivatives can be used to get a characteristic age or spin down age of the star (defined by $t_c \equiv P/2\dot{P}$) and the proper motion is used to calculate the kinetic age t_k of the star. Age (both t_k and t_c) and luminosity L data is in units of years and 10^{33} ergs/s respectively. These are converted to logarithmic scale with the new variables, $\hat{t}$ and $\hat{L}$ with their respective uncertainties $d\hat{t}$ and $d\hat{L}$

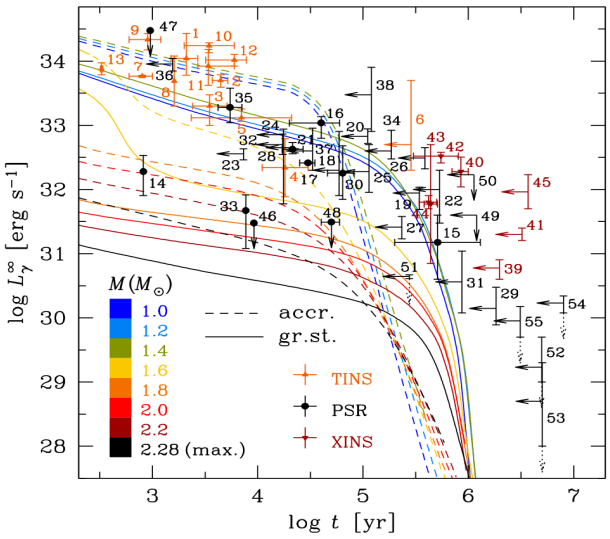

FIG. 4. Isolated Neutron stars cooling curves from [9].

as often these uncertainties are presented in logarithmic scales.

$$\hat{t} \equiv \frac{1}{5}\log_{10}\left(\frac{t}{10^2\ yr}\right)$$
$$\hat{L} \equiv \frac{1}{4}\log_{10}\left(\frac{10^{33}\ L}{10^{30}\ erg/s}\right) \tag{35}$$

This puts $\hat{t}$ in the range between 0 and 1. If the central value for the kinetic age is known, then it is used as $\hat{t}$ and the upper and lower limits of the kinetic age is used to determine $d\hat{t}$. If we do not know the age of the star accurately but we have an upper and lower bound, then the mean of these bounds are taken as $\hat{t}$ and $d\hat{t}$ is calculated as before. If no information is available about the kinetic age and only the spin-down age is known, we treat the spin-down age as an upper limit, $d\hat{t}$ is set to zero and $\hat{t}$ is set as a parameter.

The likelihood contribution from a star when both age and luminosity measurements are available is:

$$\mathcal{L}_{\mathrm{meas},j} \propto \sum_k \sqrt{\left\{\left[\frac{d\hat{L}(\eta_j)}{d\hat{t}}\right]^2 + 1\right\}} \exp\left\{\frac{-[\hat{t}_k - \hat{t}_j]^2}{2(\delta\hat{t}_j)^2}\right\} \times \exp\left\{\frac{-[\hat{L}_k(\eta_j) - \hat{L}_j]^2}{2(\delta\hat{L}_j)^2}\right\} \tag{36}$$

while k runs over a uniform grid in $\hat{t} \in [0,1]$ with grid size 100 (see [1] for details). $\hat{t}_j$ and $\hat{L}_j$ are the observed age and luminosity of the jth star. $\hat{t}_k$ and $\hat{L}_k$ are the calculated ages and luminosity at grid point k for that star.

If the age is an upper limit, the parameterized age is used to look up the luminosity from the cooling curve. In this case, there is no Gaussian contribution from age and

$$\exp\left\{\frac{-[\hat{t}_k - \hat{t}_j]^2}{2(\delta\hat{t}_j)^2}\right\} = 1, \tag{37}$$

the likelihood contribution from these stars are:

$$\mathcal{L}_{\mathrm{AUL},j} \propto \sum_k \sqrt{\left\{\left[\frac{d\hat{L}(\eta_j)}{d\hat{t}}\right]^2 + 1\right\}} \times \exp\left\{\frac{-[\hat{L}_k(\eta_j) - \hat{L}_j]^2}{2(\delta\hat{L}_j)^2}\right\} \tag{38}$$

AUL stands for age upper limit and k runs from 0 to the upper limit of that star.

A similar treatment is done to the luminosity data as well. Only this time, we do not parameterize the luminosity in case of a luminosity upper-limit star and instead just output the resulting luminosity for that particular star from our cooling calculations in our generated data files. These stars do not contribute to our likelihood functions directly for now and only act as a secondary constraint for the superfluidity and EoS in MCMC as we discard any point in the multi-dimensional parameter space that can not physically predict these stars' luminosities below the observed upper limits. So, for these luminosity upper limit (LUL) stars,

$$\begin{aligned}\mathcal{L}_{\mathrm{LUL},j} &= 0 \text{ when } \hat{L}_k > \hat{L}_j \text{ and} \\ \mathcal{L}_{\mathrm{LUL},j} &= 1 \text{ when } \hat{L}_k \le \hat{L}_j\end{aligned} \tag{39}$$

So, suppose we have N number of INSs and among them there are a number of stars of the first kind, b number of stars with age upper limits and c number of stars with luminosity upper limits such that:

$$N = a + b + c \tag{40}$$

The total likelihood contribution form N INSs look like

$$\mathcal{L}_{\mathrm{INS}} \propto \prod_{i=1}^{a} \mathcal{L}_{\mathrm{meas},i} \prod_{j=1}^{b} \mathcal{L}_{\mathrm{AUL},j} \prod_{k=1}^{c} \mathcal{L}_{\mathrm{LUL},k} \tag{41}$$

Accreting Neutron Stars

Thermal evolution of soft x-ray transient neutron stars in their quiescent phase (see Refs. [4, 30, 36, 37]) are discussed in details in Ref. [7] where the deep crustal heating [38, 39] due to accretion is radiated away by neutrino and photon emissions in its steady-state. The energy balance equation reads

$$L_h^\infty(\dot{M}) = L_\nu^\infty + L_\gamma^\infty, \tag{42}$$

The red shifted deep-crustal heating [36] is a function of the average accretion rate $\dot{M}$.

$$L_{\rm dh} = Q \times \frac{\dot{M}}{m_{\rm N}} \approx 6.03 \times 10^{33} \left(\frac{\dot{M}}{10^{-10}\,{\rm M}_\odot\,{\rm yr}^{-1}} \right) \frac{Q}{\rm MeV} {\rm ergs}^{-1} \quad (43)$$

$$L_{\rm dh}^{\infty} = L_{\rm dh}\sqrt{1-2GM/(c^2R)} \quad (44)$$

where Q is the heat released per accreted nucleon [7]. The red shifted photon and neutrino luminosities can be expressed as [7]

$$L_\gamma^\infty = 4\pi\sigma T_s^4 R^2 (1-2GM/(c^2R)) \quad (45)$$

$$L_\nu^\infty = 4\pi \int_0^R \frac{{\rm d}r r^2 \epsilon_\nu e^{2\phi(r)}}{\sqrt{1-2Gm(r)/(c^2 r)}} \quad (46)$$

solving the energy balance equation gives us the heating curves ($L_\gamma^\infty(\dot{M})$ or $T_s^\infty(\dot{M})$). We use the cooling code to achieve this as the underlying physics is still the same [36, 40].

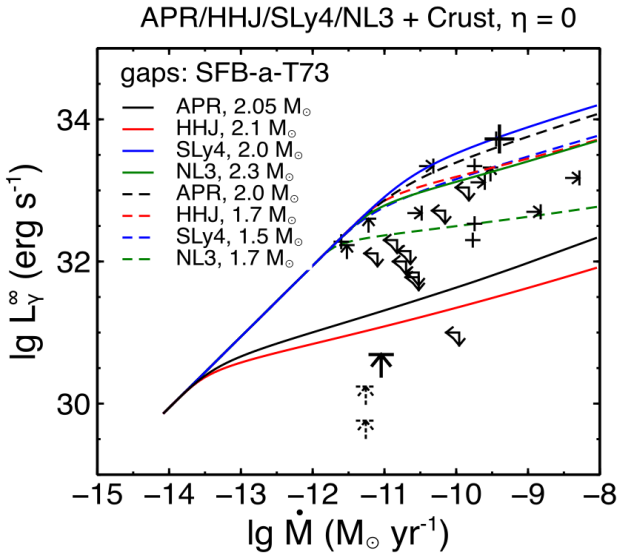

FIG. 5. Steady state curves for SXRTs from [7].

Fig. 5 is a series of selected heating curves $\log_{10}L_\gamma^\infty - \log_{10}\dot{M}$ based on EoSs in [7] with superfluidity gap models "SFB-a-T73" and observational data taken from [8, 41].

The likelihood function for SXRT stars are constructed very similarly to our isolated neutron stars approach. For these stars we have their luminosities L and accretion rates $\dot{M}$ as observed data in units of 10^{33} ergs/s and $M_\odot$/year respectively. The L and $\dot{M}$ are then converted to normalized log scale $\hat{L}$ and $\hat{\dot{M}}$.

$$\hat{L} \equiv \frac{1}{4}\log_{10}\left(\frac{10^{33}\,L}{10^{30}\,erg/s}\right) \quad (47)$$

Stellar masses and the envelop environment are parameterized as mass fraction m_f and η for the MCMC. For very cold SXRTs SAX J1808.4-3658 [41, 42] and 1H 1905+000 [43], only the upper limits of luminosities are known. And in addition, for 1H 1905+000, $\dot{M}$ only provides an upper limit. These are also parameterized in the MCMC with appropriate uncertainties.

The cooling code calculates the steady-state curves for stars with masses ranging from 1-2 $M_\odot$, η ranging from $10^{-17} - 10^{-7}$ and $\dot{M}$ ranging from $10^{-14} - 10^{-8}$. These results are stored into a 3-dimensional tensor grid which we use to interpolate and get luminosity for all different combinations of m, η and $\dot{M}$.

Following Ref. [7] the likelihood contribution from each SXRT star for which luminosity and accretion rate are known measurements look like

$$\mathcal{L}_{{\rm meas},j} \propto \sum_k \sqrt{\left\{\left[\frac{d\hat{L}(\eta_j)}{d\hat{\dot{M}}}\right]^2 + 1\right\}} \times \exp\left\{\frac{-[\hat{\dot{M}}_k - \hat{\dot{M}}_j]^2}{0.5}\right\} \times \exp\left\{\frac{-[\hat{L}_k(\eta_j) - \hat{L}_j]^2}{0.5}\right\} \quad (48)$$

where $\hat{L}_k$ and $\hat{\dot{M}}_k$ are the interpolated and $\hat{L}_j$ and $\hat{\dot{M}}_j$ are the observed luminosity and accretion rates respectively. k runs over a uniform grid $[-12, 29]$ for $\log_{10}(\dot{M})$.

For SAX J1808 as the luminosity is an upper limit, there is no Gaussian contribution from luminosity as long as the calculated luminosity is under the upper limit.

$$\exp\left\{\frac{-[\hat{L}_k(\eta_{1808}) - \hat{L}_{1808}]^2}{0.5}\right\} = 1 \text{ if } \hat{L}_k \le \hat{L}_{1808}$$
$$\exp\left\{\frac{-[\hat{L}_k(\eta_{1808}) - \hat{L}_{1808}]^2}{0.5}\right\} = 0 \text{ if } \hat{L}_k > \hat{L}_{1808} \quad (49)$$

and

$$\mathcal{L}_{1808} \propto \sum_k \sqrt{\left\{\left[\frac{d\hat{L}(\eta_{1808})}{d\hat{\dot{M}}}\right]^2 + 1\right\}} \times \exp\left\{\frac{-[\hat{\dot{M}}_k - \hat{\dot{M}}_{1808}]^2}{0.5}\right\} \quad (50)$$

Similarly for 1H 1905, both luminosity and accretion rates are upper limits and hence both Gaussian contribute nothing when the calculated values are higher

than their upper limits.

$$\exp\left\{\frac{-[\hat{L}_k(\eta_{1905})-\hat{L}_{1905}]^2}{0.5}\right\}=1 \text{ if } \hat{L}_k\leq\hat{L}_{1905}$$
$$\exp\left\{\frac{-[\hat{L}_k(\eta_{1905})-\hat{L}_{1905}]^2}{0.5}\right\}=0 \text{ if } \hat{L}_k>\hat{L}_{1905} \quad (51)$$

and

$$\exp\left\{\frac{-[\hat{\dot{M}}_k-\hat{\dot{M}}_{1905}]^2}{0.5}\right\}=1 \text{ if } \hat{\dot{M}}_k\leq\hat{\dot{M}}_{1905}$$
$$\exp\left\{\frac{-[\hat{\dot{M}}_k-\hat{\dot{M}}_{1905}]^2}{0.5}\right\}=0 \text{ if } \hat{\dot{M}}_k>\hat{\dot{M}}_{1905} \quad (52)$$

So

$$\mathcal{L}_{1905}\propto\sum_k\sqrt{\left\{\left[\frac{d\hat{L}(\eta_{1905})}{d\hat{\dot{M}}}\right]^2+1\right\}} \quad (53)$$

So the total likelihood contribution form SXRT stars look like

$$\mathcal{L}_{\rm SXRT}\propto\prod_j\mathcal{L}_{{\rm meas},j}\times\mathcal{L}_{1808}\times\mathcal{L}_{1905} \quad (54)$$

QLMXB stars

Just like SXRTs low-mass X-ray binaries (LMXBs) have periods of accretion and quiescence. This accreted mass in the higher mass star causes energy outbursts that are observable in X-ray regime and have really high luminosities [44].

We use the results obtained from the seven QLMXBs in the data set from Ref. [44] (see the references therein) and the same likelihood used in [1] (see Eq. 102 of Ref. [22]). The masses and the atmosphere of the stars are parameterized as m_f and ζ_i in the MCMC. This ζ is a random number between 0 and 1 for each star. If $\zeta<2/3$ a hydrogen atmosphere is chosen for the star and if $\zeta>2/3$ a helium atmosphere is preferred. Their masses range from 1 $M_\odot$ to the maximum mass predicted by the TOV solver for our EoS. This works contains more recent data for M30 and two new NICER objects PSR J0030+0451 [45] and PSR J0740+6620 [46]. However due to some technical difficulties, M30 is currently omitted from our calculations which we hope to fix in the near future.

The likelihood function for QLMXB stars

$$\mathcal{L}_{\rm QLMXB} = \prod_{i=1}^{8}\{\theta(2/3-\zeta_i)\mathcal{D}_{i,\rm H}[R(M_i),M_i] + \theta(\zeta_i-2/3)\mathcal{D}_{i,\rm He}[R(M_i),M_i]\} \quad (55)$$

where M_i is the mass of the ith star, ζ_i are the atmosphere parameter, R_i are the radius, $\mathcal{D}_{i,\rm H}$ and $\mathcal{D}_{i,\rm He}$ are the probability distributions considering either a hydrogen or a helium atmosphere (see Ref. [1] for details).

LIGO

For the neutron stars in GW170817 [10], we use kernel density estimation to convert the Monte Carlo samples from Ref. [47] to a three-dimensional probability distribution over $M_{\rm chirp}$, q, and $\tilde{\Lambda}$. The masses of the two neutron stars involved in the merger are sampled from a uniform distribution from 1 solar mass to the maximum mass. The tidal deform-ability for the two neutron stars is computed from the moment of inertia using Yagi-Yunes correction [48] as formulated in [49].

MCMC

With the individual likelihood contributions in place, our full likelihood function looks like

$$\mathcal{L}=\mathcal{L}_{\rm nuclei}\mathcal{L}_{\rm LIGO}\mathcal{L}_{\rm INS}\mathcal{L}_{\rm QLMXB}\mathcal{L}_{\rm SXRT} \quad (56)$$

Given the prior distributions $P(M)$ of our 151 parameters, the likelihood function is the probability of the data given the model $P(D|M)$. Once we compute the likelihood for a model, Bayesian equation gives us the probability of the model given the data [1].

$$P(M|D)\propto P(D|M)P(M) \quad (57)$$

We use Markov chain Monte Carlo (MCMC) method to sample from this distribution of our large dimensional parameter space. Either the Metropolis-Hastings algorithm or the affine-invariant sampling (Goodman and Weare) is used to obtain sequences of random samples of parameters from this distribution and the likelihood is computed satisfying all the physics constraints. The MCMC goes through an accept-reject and a measurement step at each point until the entire MCMC process is done [13].

RESULTS

Table. I has brief descriptions of all of our MCMC parameters. While using the Metropolis-Hastings algorithm, we used both random-walk step and Gaussian proposal distributions for the parameters in MCMC. From our results, the Gaussian distribution seems to equilibriate or match the desired distribution sooner. We want to find an EoS that can explain all of these stars to a reasonable accuracy and in the process, shade some light onto the superfluidity conditions inside these stars. After running the MCMC for large period of time we want to create a large enough data set for our emulators which will eventually replace the physical calculations and based on the input parameters from the MCMC will accurately predict the outputs we are looking for.

Our simulations with RMF EoSs tend to suggest stars with larger radii are more probabilistic as there are very

Parameter	Description
$\log_{10} T_{c,\mathrm{peak},n}$	Critical temperature for neutrons
$k_{F,\mathrm{peak},n}$ (fm^{-1})	Peak Fermi-momenta for neutrons
$\Delta k_{F,n}$ (fm^{-1})	Width of the Gaussian for neutrons
$\log_{10} T_{c,\mathrm{peak},p}$	Critical temperature for protons
$k_{F,\mathrm{peak},p}$ (fm^{-1})	Peak Fermi-momenta for protons
$\Delta k_{F,p}$ (fm^{-1})	Width of the Gaussian for protons
c_ρ, c_σ, c_ω	the meson-nucleon couplings
m_σ	the σ meson mass
b, c, ζ, ξ	meson couplings from Ref. [50]
$b_{1,2,3}$ and $a_{1,2,3,4,5,6}$	higher-order meson couplings from Ref. [17]
α	The direct Urca broadening parameter
Q	The heating parameter
M_{chirp}, q, $\tilde{\Lambda}$	The chirp mass, mass ratio and tidal deformability from GW 170817
$m_{f,i}$	masses of the stars parameterized as mass fraction
η_i	atmosphere parameter of the INS and SXRTs
ζ_i	atmosphere parameter for QLMXB stars

TABLE I. Parameter set for our MCMC and their brief descriptions

Star	L_{Beloin}	L_{NSC}	$\frac{L_{\mathrm{Bel}}-L_{\mathrm{NSC}}}{\sqrt{\sum dL^2}}$	T_{Beloin}	T_{Beznogov}	$\frac{T_{\mathrm{Bel}}-T_{\mathrm{Bez}}}{\sqrt{\sum dT^2}}$	$L_{\mathrm{Beloin-calc}}$
Cas A	$33.63^{+0.08}_{-0.08}$	$33.5^{+0.1}_{-0.1}$	1.015	$6.26^{+0.02}_{-0.02}$	6.204	2.8	
J1732	$33.99^{+0.03}_{-0.03}$			$6.25^{+0.0073}_{-0.0073}$	$6.253^{+0.007}_{-0.007}$	-0.296	
J1119	$33.32^{+0.14}_{-0.14}$	$33.25^{+0.15}_{-0.15}$	0.341	$6.09^{+0.08}_{-0.08}$	6.079	0.138	
J0822	$33.93^{+0.08}_{-0.08}$	$33.6^{+0.1}_{-0.1}$	2.577	$6.24^{+0.04}_{-0.04}$	$6.242^{+0.04}_{-0.04}$	-0.035	
1207	$33.50^{+0.24}_{-0.24}$	$33.5^{+0.5}_{-0.5}$	0.0	$6.21^{+0.07}_{-0.07}$			
J1357	$32.63^{+0.17}_{-0.17}$			$5.88^{+0.04}_{-0.04}$	5.886	-0.15	
B0833	$32.58^{+0.04}_{-0.04}$	$32.2^{+0.1}_{-0.1}$	3.528	$5.83^{+0.02}_{-0.02}$	$5.832^{+0.02}_{-0.02}$	-0.071	
B1706	$32.47^{+0.56}_{-0.56}$	$31.9^{+0.2}_{-0.2}$	0.790	$5.80^{+0.13}_{-0.13}$	$5.80^{+0.119}_{-0.119}$	0.0	
J0538	$33.10^{+0.50}_{-0.50}$	$32.8^{+0.1}_{-0.1}$	0.588	$6.05^{+0.1}_{-0.1}$	5.939	1.11	
B2334	$32.70^{+0.68}_{-0.68}$	$30.9^{+0.2}_{-0.2}$	2.539	$5.68^{+0.17}_{-0.17}$	5.839	-0.935	
B0656	$32.58^{+0.40}_{-0.40}$	$32.75^{+0.05}_{-0.05}$	-0.422	$5.71^{+0.035}_{-0.035}$	5.898	-5.371	$31.825^{+0.325}_{-0.325}$
J1740	$32.15^{+0.05}_{-0.05}$	$32.15^{+0.05}_{-0.05}$	0.0	$6.04^{+0.01}_{-0.01}$			$32.78^{+0.04}_{-0.04}$
B0633	$31.18^{+0.33}_{-0.33}$			$5.75^{+0.045}_{-0.045}$	$5.69^{+0.088}_{-0.088}$	0.607	$31.6^{+0.18}_{-0.18}$
J1856	$31.56^{+0.12}_{-0.12}$	$31.6^{+0.1}_{-0.1}$	-0.256	$5.75^{+0.15}_{-0.15}$	$5.637^{+0.003}_{-0.003}$	0.753	$31.99^{+0.59}_{-0.59}$
B1055	$32.57^{+0.52}_{-0.52}$	$32.4^{+0.2}_{-0.2}$	0.305	$5.88^{+0.08}_{-0.08}$	5.875	0.063	$32.43^{+0.32}_{-0.32}$
J2043	$29.62^{+0.52}_{-0.52}$			$5.64^{+0.08}_{-0.08}$	5.643	-0.037	
J0720	$31.89^{+0.52}_{-0.52}$	$32.3^{+0.1}_{-0.1}$	-0.774	$5.75^{+0.02}_{-0.02}$	5.707	0.215	$31.82^{+0.9}_{-0.9}$

TABLE II. Data comparison between Beloin, Beznogov and `neutronstarcooling.info`

small number of points that has smaller radii for 1.4 $M_\odot$ stars with a reasonable likelihood. This is in direct contradiction of the LIGO results that tends to prefer smaller radii. This might be because the MCMC is stuck at a local maxima and is not properly exploring the entirety of the parameter space. This is a problem for our emulators as it also needs enough information for the small radius data set to accurately predict the results when these points arise in the MCMC.

This is a motivation to try out known RMF models like SFHo, SFHx or IUFSU EoSs as they have historically predicted smaller radius for 1.4 $M_\odot$ neutron stars. SFHo and SFHx do not support direct-Urca for standard nuclear matter and hence are poor when it comes to explaining cold accreting stars. IUFSU on the other hand produces nuclear properties pretty well but It has no higher order meson couplings from Ref. [17]. IUFSU has small radii predictions for 1.4 $M_\odot$ neutron star $\sim$ 12.6 km but it limits the maximum mass of a neutron star from the TOV-solver to $\sim 1.93 M_\odot$ when we are looking to at least solve for 2 $M_\odot$ neutron stars. We let the equation of state parameters to sit very close to the IUFSU model and then let the additional couplings from Ref. [17] vary within their theoretical upper and lower limits to run free until we get a satisfactory initial point for our MCMC. Subsequent points provide enough data for small radii that we can use to train our emulators.

Depending on how good RMF EoSs for standard nuclear matter explain these stars will tell us if we need the presence of more exotic matter like Hyperons or quarks in these stars to explain them better.

In fig. 6 we have the isolated neutron stars' cooling curves from Ref. [9]. With our current IUFSU like EoS with added meson interactions. Here we have manually

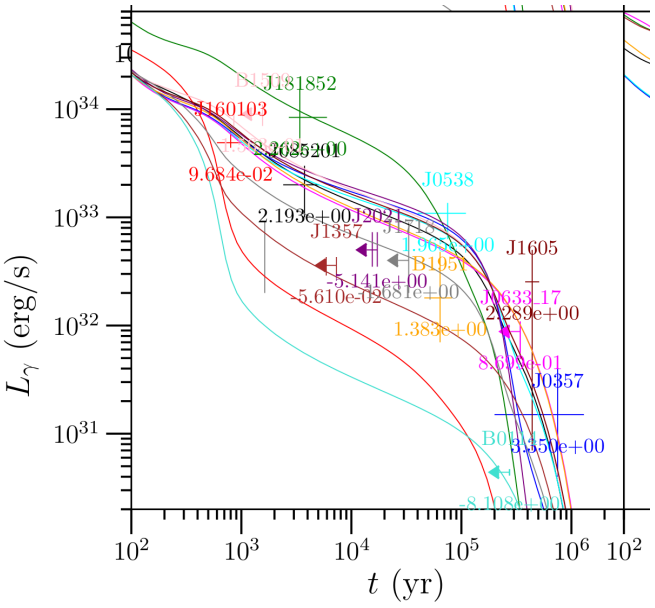

FIG. 6. INS cooling curve with an IUFSU like EoS

restricted the 1.4 $M_\odot$ neutron star radius to be < 12.75 km. The data point are from Ref. [35] with their individual log likelihoods computed using the techniques mentioned above. Some stars like J141256 or J1308 are particularly difficult to fit and may require us to parameterize their magnetic fields in our codes. We can see that the lower mass stars cool via the minimal cooling processes and the really high mass stars have direct-Urca enabling them to cool rapidly giving us the low luminosity we observe for the stars like B2334 or B0114.

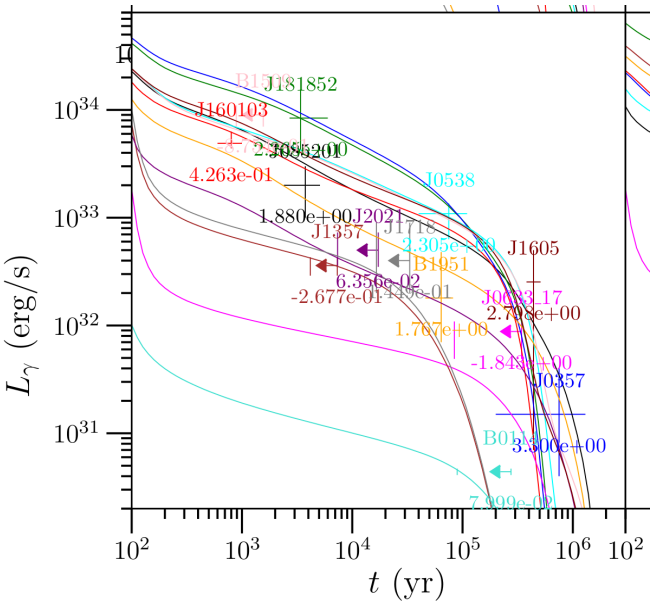

FIG. 7. INS cooling curve with a free RMF EoS

In fig. 7 we have the same stars as in fig. 6 but we are using a free RMF EoS without the radial constraint. The simulation is much more likely to be successful this way and will skip less number of points in the parameter space.

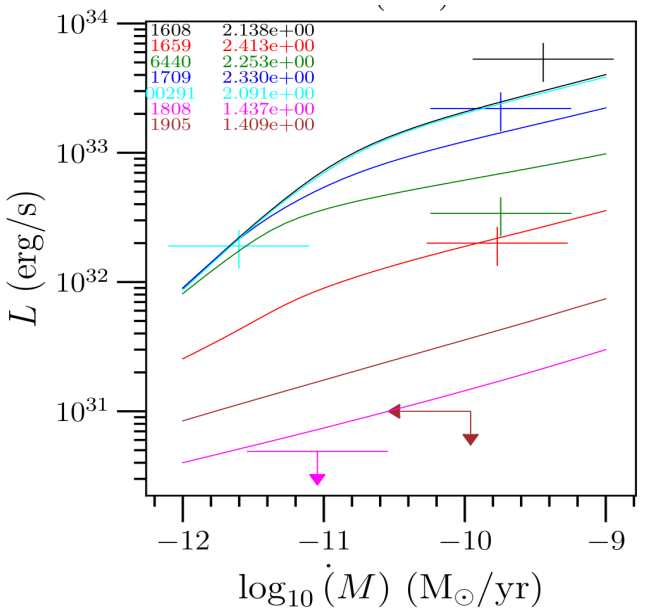

FIG. 8. SXRT heating curves with an IUFSU like EoS

In fig. 8 we have our accreting neutron stars heating curves $L_\gamma^\infty - \dot{M}$ with their individual log likelihoods. It is rather difficult to fit cold stars like J1808 or J1905 with this model and most points end up getting rejected or with pretty low likelihoods.

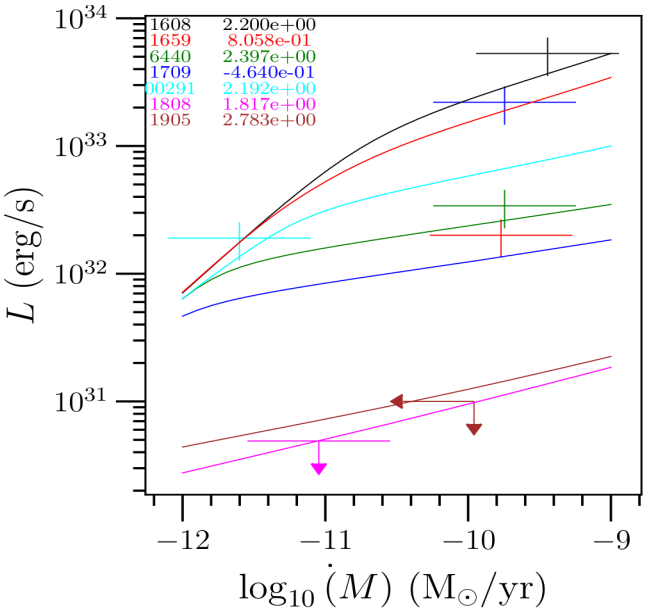

FIG. 9. SXRT heating curves with a free RMF EoS

Fig. 9 depicts the steady-state curves without the EoS or radial restrictions. The model has the flexibility to explain the colder stars much better.

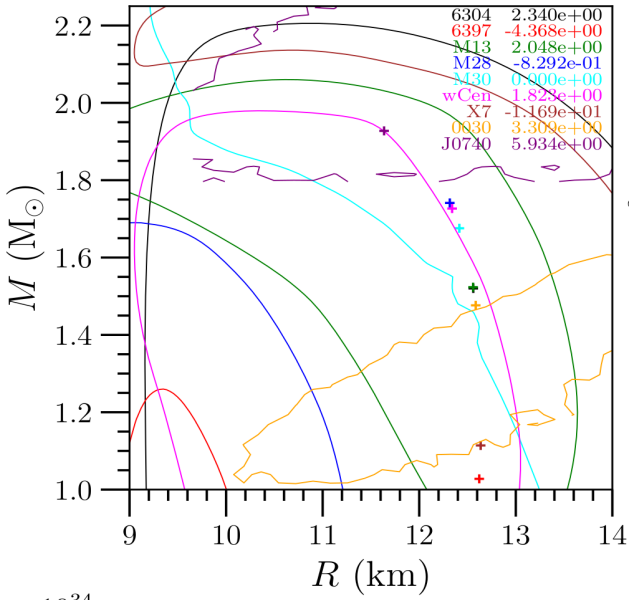

FIG. 10. M-R curves of QLMXB stars with an IUFSU like EoS

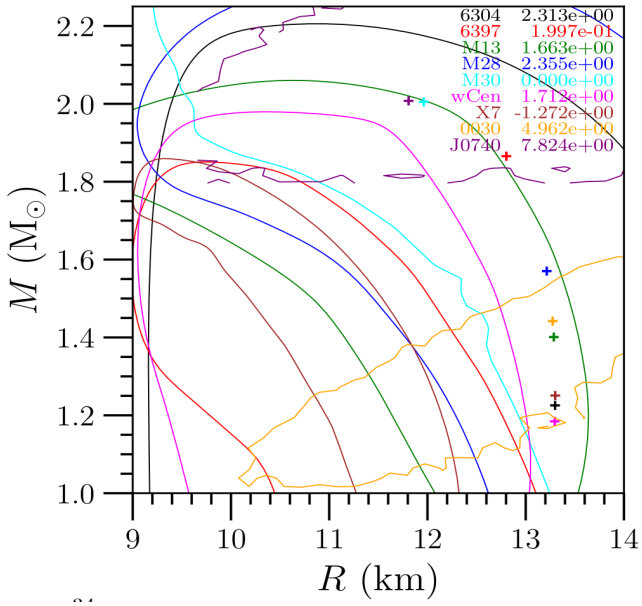

FIG. 11. M-R curves of QLMXB stars with a free RMF EoS

Fig. 10 and fig. 11 are the M-R contour plots for QLMXB stars with their likelihoods shown at the top right corners for IUFSU like and the free RMF EoSs respectively. Fig. 12 and fig. 13 are the tidal deformability vs the mass ratio density plots for GW170817 for each of these cases.

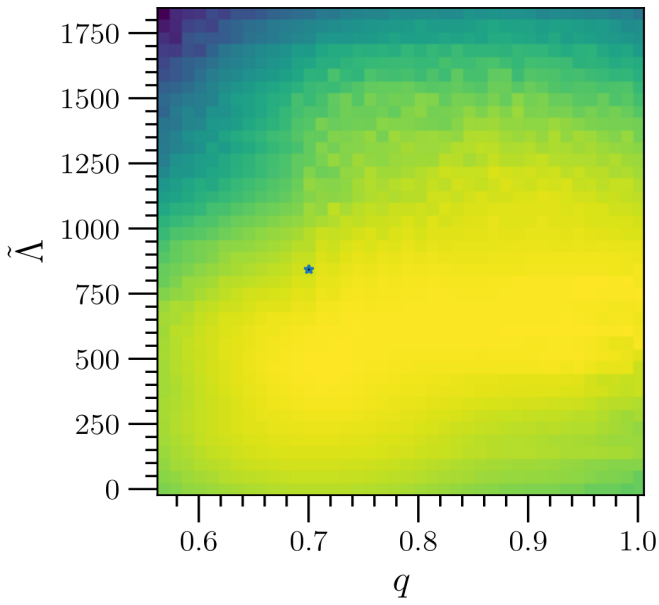

FIG. 12. Tidal deformability plot with an IUFSU like EoS

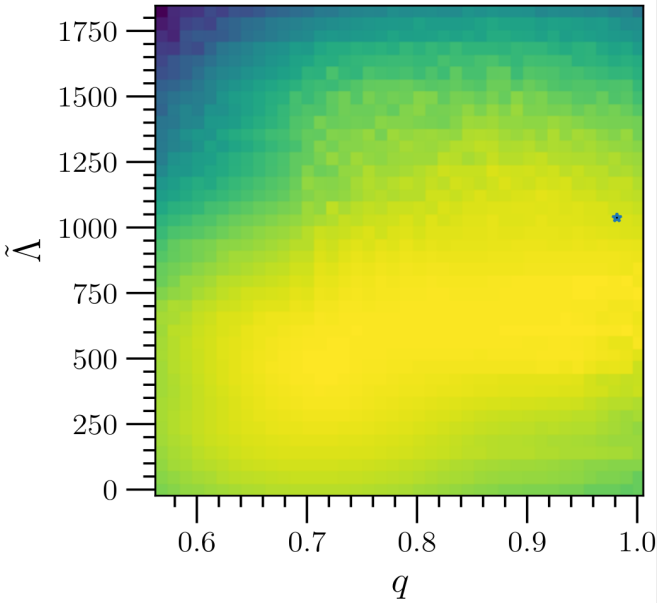

FIG. 13. Tidal deformability plot with a free RMF EoS

For the SXRTs, SAX-1808 and 1905 are the two most difficult stars to fit as their luminosity is extremely low. It is not possible to reach their low luminosity with the minimal cooling scenario and we must have direct-Urca process in the core to explain these stars.

Fig. 10 shows the density plots for the QLMXB stars for a different low radii point. M30 is particularly problematic as the density plot suggests. M30 has low mass low radii data which seems unreasonable from our calculations as lower mass neutron stars tend to have a larger radius due to lower gravitational pull.

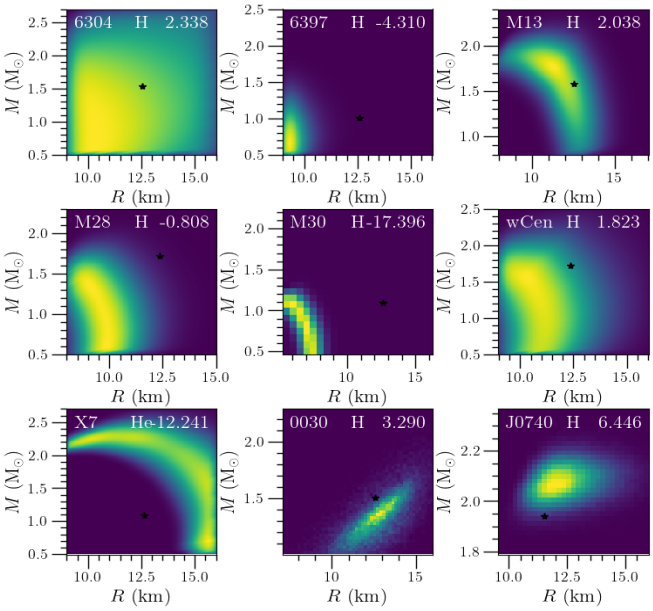

FIG. 14. QLMXB density plots with smaller radii data

Table. II summarizes the differences between the data in Refs. [1], [9] and [8] with their uncertainties. Here we have a brief comparison between of the common data available in these papers. While Ref. [9] provides the luminosity data, Ref. [8] has the temperature data. Considering the uncertainties, we see some stars don't agree when we do an error analysis. B0833 have a higher uncertainty in recent studies compared to Ref. [1]. J0822 and B2334 shows a similar trend as well and have lower luminosities when compared to Ref. [1]. B0833 and J0822 are slowly cooling stars that can be explained by minimal cooling models but B2334 is a cold star that needs fast cooling processes to be explained properly. When we compare the temperature data, we see the outliers being Cas A and B0656. While most of the error comes from the lack of uncertainties in Ref. [8], Cas A is a new and hot star (easily explained by minimal cooling), B0656 is an old star that is still pretty hot. We might need to consider larger magnetic fields or reheating to account for its temperature.

ONGOING WORK

Currently we are generating data sets with IUFSU like EoSs to have a larger data set for our emulators. We are looking to implement a number of emulators and see what produces the best results. These include an inverse-distance-weighted interpolation (IDW) emulator, a Gaussian process regression (GPR) emulator and a deep-neural-network (DNN) emulator. Each of these comes with its own set of challenges.

GPR model is based on [51] and we use the library from scikit-learn. Gaussian processes have a lot of advantages making it a versatile tool for our job, however it loses efficiency in high dimensional space, which is our case. We choose to use the Radial-basis function kernel for our GPR model. The DNN emulator uses the `tensorflow` library. It is currently a `sequencial` model with three layers (`tanh, tanh, sigmoid`) and the `adam` optimizer. While it has large success rate and great accuracy, it has issues with the physically improbable points and predicts them wrong at times. We hope to fix this in the near future.

In this paper we would like to finish our work by this fall semester with our RMF EoSs to better constraint the superfluidity parameters and find an EoS parameterizations that is well-suited to explain the multi-messenger observations that is available to us. We would like to fix the new M30 data inconsistency issue so we can include it in our calculations. Most importantly we want to create a framework that is scalable into the future so we can add new observations with minimal efforts to update the results.

FUTURE WORK

Hyperons can form in neutron star cores when the nucleon chemical potentials grow large enough ($\rho_B = 2\rho_0$) to compensate for the mass differences between nucleons and hyperons. [52] discuses presence and roles of hyperons in neutron stars in a detailed manner. The presence of hyperon softens the EoS compared to a pure nuclear-matter EoS [53]. Creation of hyperons as an additional species inside a NS relieve some of the Fermi pressure of the nucleons and sort of acts like a "pressure control" mechanism in high density matter. [52]. Hyperons also affect the maximum mass of an EoS as well by making it lower. Having hyperons inside the core affects the cooling process significantly as well by opening up the hyperonic direct-Urca channels, this might be helpful in explaining the extremely low luminosity stars in our studies like J1808 or 1905.

In our next project, We would like to include hyperons in our calculations and see how that affects our results.

THANKS

We thank Dany Page for his wonderful `NSCool` cooling code for neutron stars. We are thankful for the computational resources from the University of Tennessee to run our MCMC simulations.

[1] S. Beloin, S. Han, A. W. Steiner, and K. Odbadrakh, Phys. Rev **C 100**, 055801 (2019), URL https://doi.org/10.1103/PhysRevC.100.055801.

[2] J. M. Lattimer and M. Prakash, Astrophys. J. **550**, 426 (2001), URL https://doi.org/10.1086/319702.

[3] D. Page, J. M. Lattimer, M. Prakash, and A. W. Steiner, The Astrophysical Journal **155**, 623 (2004), URL https://doi.org/10.1086/424844.

[4] C. O. Heinke, P. G. Jonker, R. Wijnands, and R. E. Taam, Astrophys. J. **660**, 1424 (2007), URL https://doi.org/10.48550/arXiv.astro-ph/0612232.

[5] A. B. Migdal, Nuclear Phys **13-5**, 655 (1959), URL https://doi.org/10.1016/0029-5582(59)90264-0.

[6] D. Page, J. M. Lattimer, M. Prakash, and A. W. Steiner, *Stellar Superfluids* (2014), chap. 21, ISBN 9780198719267, 1302.6626.

[7] S. Han and A. W. Steiner, Phys. Rev **C 96**, 035802 (2017), URL https://doi.org/10.48550/arXiv.1702.08452.

[8] M. V. Beznogov and D. G. Yakovlev, MNRAS **447**, 1598 (2015), URL https://doi.org/10.48550/arXiv.1411.6803.

[9] A. Y. Potekhin, D. A. Zyuzin, D. G. Yakovlev, M. V. Beznogov, and Y. A. Shibanov, MNRAS **496**, 5052 (2020), URL https://doi.org/10.48550/arXiv.2006.15004.

[10] B. P. Abbott et al., Phys. Rev. Lett. **119**, 161101 (2017), URL https://doi.org/10.1103/PhysRevLett.119.161101.

[11] P. G. Reinhard, X. R. Maza, and W. Nazarewicz, Phys. Rev. Lett. **127**, 232501 (2021), URL https://doi.org/10.1103/PhysRevLett.127.232501.

[12] D. Page (2010), URL http://www.astroscu.unam.mx/neutrones/NSCool/NSCool_Guide_1.1_Introduction.pdf.

[13] A. W. Steiner (2022), URL https://neutronstars.utk.edu/code/o2scl/html/index.html.

[14] B. Schutz, *A First Course in General relativity* (2011).

[15] G. F. Burgio and A. F. Fantina, The Physics and Astrophysics of Neutron Stars **Astrophysics and Space Science Library Book 457, Springer** (2018), URL https://doi.org/10.48550/arXiv.1804.03020.

[16] B. D. Serot and J. D. Walecka, *Relativistic Nuclear Many-Body Theory* (1986), vol. 16, p. 1.

[17] A.W.Steiner, M.Prakash, J.M.Lattimer, and P.J.Ellis, Physics Reports **411-6**, 325 (2005), URL https://doi.org/10.1016/j.physrep.2005.02.004.

[18] N. K. Glendenning, *Compact stars* (Springer, 2000), 2nd ed.

[19] F. Weber, R. Negreiros, P. Rosenfield, and M. Stejner, Prog.Part.Nucl.Phys **59**, 94 (2007), URL https://doi.org/10.1016/j.ppnp.2006.12.008.

[20] J. P. W. Diener, *Relativistic Mean-Field Theory Applied To The Study Of Neutron Star Properties* (Stellenbosch University, 2008), chap. Thesis (MSc (Physics).

[21] J. M. Lattimer and M. Prakash, Phys. Rep. **442**, 109 (2007), URL https://doi.org/10.48550/arXiv.astro-ph/0612440.

[22] J. M. Lattimer and A. W. Steiner, The European Physical Journal A **50**, 40 (2014), URL https://doi.org/10.48550/arXiv.1403.1186.

[23] U. Garg and G. Colò, Prog.Part.Nucl.Phys **101**, 55 (2018), URL https://doi.org/10.1016/j.ppnp.2018.03.001.

[24] C. Horowitz and B. D. Serot, Nuclear Physics **A368**, 503 (1981), URL https://doi.org/10.1016/0375-9474(81)90770-3.

[25] V. Thakur and S. K. Dhiman, Nuclear Phys A **992**, 121623 (2019), URL https://doi.org/10.1016/j.nuclphysa.2019.121623.

[26] D. Adhikari and others (PREX Collaboration), Phys. Rev. Lett. **126**, 172502 (2021), URL https://doi.org/10.48550/arXiv.2102.10767.

[27] J. W. Negele and D. Vautherin, Nucl. Phys. **A207**, 298 (1973), URL https://doi.org/10.1016/0375-9474(73)90349-7.

[28] C. Pethick, D.G.Ravenhall, and C.P.Lorenz, Nuclear Physics A **584**, 675 (1995), URL https://doi.org/10.1016/0375-9474(94)00506-I.

[29] D. Yakovlev, A. Kaminker, O. Gnedin, and P. Haensel, Physics Reports **354**, 1 (2001), URL https://doi.org/10.48550/arXiv.astro-ph/0012122.

[30] D. Yakovlev and C. Pethick, Annu. Rev. Astron. Astrophys. **42**, 169 (2004), URL https://doi.org/10.48550/arXiv.astro-ph/0402143.

[31] E. H. Gudmundsson, C. J. Pethick, and R. I. Epstein, Astrophysical Journal **272**, 286 (1983), URL https://ui.adsabs.harvard.edu/abs/1983ApJ...272..286G/abstract.

[32] S. Beloin, S. Han, A. W. Steiner, and D. Page, Phys Rev p. 97 (2018), URL https://doi.org/10.48550/arXiv.1612.04289.

[33] S. L. Shapiro and S. A. Teukolsky, *Black holes, white dwarfs, and neutron stars : the physics of compact objects* (1983), ISBN 9780471873167.

[34] D. Page, J. M. Lattimer, M. Prakash, and A. W. Steiner, The Astrophysical Journal **707**, 1131 (2009), URL https://doi.org/10.48550/arXiv.0906.1621.

[35] A. Potekhin, D. Zyuzin, D. Yakovlev, M. Beznogov, and Y. Shibanov., MNRAS **496**, 5052 (2020), URL http://www.ioffe.ru/astro/NSG/thermal/cooldat.html.

[36] D. G. Yakovlev, K. P. Levenfish, and P. Haensel, Astronomy and Astrophysics **407**, 265 (2003), URL https://doi.org/10.1051/0004-6361:20030830.

[37] D.G.Yakovlev, K.P.Levenfish, A.Y.Potekhin, O.Y.Gnedin, and G.Chabrier, A&A **417**, 169 (2004), URL https://doi.org/10.1051/0004-6361:20034191.

[38] P. Haensel and J. L. Zdunik, Astron. Astrophys. **227**, 431 (1990), URL https://articles.adsabs.harvard.edu/pdf/1990A%26A...227..431H.

[39] P. Haensel and J. Zdunik, Astrophysical Journal **404**, L33 (2003), URL https://doi.org/10.1051/0004-6361:20030708.

[40] C. M., G. U., P. D., and P. A., Astrophysical Journal **548**, 175 (2001), URL https://iopscience.iop.org/article/10.1086/319107/pdf.

[41] C. O. Heinke, D. Altamirano, H. N. Cohn, P. M. Lugger, S. A. Budac, M. Servillat, M. Linares, T. E. Strohmayer, C. B. Markwardt, and R. Wijnands, **714**, 894 (2010), URL https://doi.org/10.1088/0004-637x/714/1/894.

[42] S. Campana, L. Stella, F. Gastaldello, S. Mereghetti, M. Colpi, G. L. Israel, L. Burderi, T. D. Salvo, and R. N. Robba, The Astrophysics Journal **575**, L15 (2002), URL https://doi.org/10.1086/342505.

[43] P. G. Jonker, D. Steeghs, D. Chakrabarty, and A. M. Juett, The Astrophysical Journal **665**, L147 (2007), URL https://doi.org/10.1086/521079.

[44] A. W. Steiner, C. O. Heinke, S. Bogdanov, C. K. Li, W. C. G. Ho, A. Bahramian, and S. Han, Monthly Notices of the Royal Astronomical Society **476**, 421 (2018), URL https://doi.org/10.1093/mnras/sty215.

[45] M. C. Miller, F. K. Lamb, A. J. Dittmann, S. Bogdanov, Z. Arzoumanian, K. C. Gendreau, S. Guillot, A. K. Harding, W. C. G. Ho, J. M. Lattimer, et al., The Astrophysical Journal **887**, L24 (2019), URL https://doi.org/10.3847/2041-8213/ab50c5.

[46] M. T. Wolff, S. Guillot, S. Bogdanov, P. S. Ray, M. Kerr, Z. Arzoumanian, K. C. Gendreau, M. C. Miller, A. J. Dittmann, W. C. G. Ho, et al., **918**, L26 (2021), URL https://doi.org/10.3847/2041-8213/ac158e.

[47] B. P. Abbott et al. (2017), URL https://dcc.ligo.org/LIGO-P1800061/public.

[48] K. Yagi and N. Yunes, Classical and Quantum Gravity **34**, 015006 (2016), URL https://doi.org/10.1088/1361-6382/34/1/015006.

[49] K. Yagi and N. Yunes, Phys. Rev **D 88**, 023009 (2013), URL https://doi.org/10.1103/PhysRevD.88.023009.

[50] H. Muller and B. D. Serot, Nucl.Phys. **A606**, 508 (1996), URL https://doi.org/10.48550/arXiv.nucl-th/9603037.

[51] C. E. Rasmussen and C. K. Williams, *Gaussian Processes for Machine Learning* (MIT Press, 2006).

[52] S. Balberg and I. Lichtenstadt, The Astrophysical Journal Supplement Series **121**, 515 (1999), URL https://doi.org/10.48550/arXiv.astro-ph/9810361.

[53] N. K. Glendenning, *Compact Stars* (Springer, 1996).